
GAUSSIAN PROCESS REGRESSION FOR ESTIMATING EM DUCTING WITHIN THE MARINE ATMOSPHERIC BOUNDARY LAYER

A PREPRINT

Hilarie Sit
Civil and Environmental Engineering
Cornell University
Ithaca, NY 14853
hs764@cornell.edu

Christopher J. Earls
Civil and Environmental Engineering
Center for Applied Mathematics
Cornell University
Ithaca, NY 14853

September 2, 2022

ABSTRACT

We show that Gaussian process regression (GPR) can be used to infer the electromagnetic (EM) duct height within the marine atmospheric boundary layer (MABL) from sparsely sampled propagation factors within the context of bistatic radars. We use GPR to calculate the posterior predictive distribution on the labels (*i.e.* duct height) from both noise-free and noise-contaminated array of propagation factors. For duct height inference from noise-contaminated propagation factors, we compare a naïve approach, utilizing one random sample from the input distribution (*i.e.* disregarding the input noise), with an inverse-variance weighted approach, utilizing a few random samples to estimate the true predictive distribution. The resulting posterior predictive distributions from these two approaches are compared to a “ground truth” distribution, which is approximated using a large number of Monte-Carlo samples. The ability of GPR to yield accurate duct height predictions using few training examples, along with its inference speed, indicates the suitability of the proposed method for real-time applications.

1 Introduction

Turbulent transport of momentum, moisture, and heat between the ocean and the atmosphere characterizes the marine atmospheric boundary layer (MABL) - the region in the lower troposphere that is in direct contact with the ocean surface (Sikora and Ufermann, 2004). Inhomogeneity in pressure, humidity, and temperature can result in anomalous propagation of electromagnetic (EM) waves. Behavior of EM wave propagation is influenced by the index of refraction, which is the speed of light in medium relative to that in vacuum, that is dependent on spatial variations in atmospheric conditions. Rapid decrease in the index of refraction with increasing altitude can create a “trapping” layer where EM waves are refracted back toward the ocean surface. This phenomenon, called *atmospheric ducting*, can impact performance of radar and communication systems by causing unexpected holes in coverage, inaccurate measurement of elevation angle, and extension of radar horizon (Skolnik, 1980). The index of refraction within the MABL may be assumed to be stationary for up to several minutes (Rogers, 1996). Thus, it is of great interest to devise real-time methods that can accurately identify and characterize these EM ducts within a few minutes of an EM propagation measurement, so that, for instance, radar operators can be informed about their system expected performance in real-time.

One method for estimating duct characteristics is by calculating the index of refraction using direct measurements of atmospheric conditions within the MABL (*e.g.* temperature, pressure, and humidity). The refractivity profile can be written as an empirical equation parameterized by atmospheric temperature, pressure, and humidity, which can be measured via radiosondes or rocketsondes (Bean and Dutton, 1968). However, direct measurements of atmospheric conditions are necessarily sparse and implementation can be expensive, rendering this method impractical for real-time

estimation of MABL refractivity. Other methods for EM duct estimation include using GPS (Lowry et al., 2002) and LIDAR (Willitsford and Philbrick, 2005) measurements to estimate the index of refraction. However, both methods are not practical in the context of the duct characterization problem, because GPS performance is dependent on favorable satellite alignment over the horizon and LIDAR performance is dependent on favorable weather conditions.

More recently, refractivity from clutter (RFC) methods have gained traction in the literature. RFC methods use radars to measure clutter (*i.e.* backscattered power from the rough ocean surface); thus employing backscattered returns to estimate the refractivity (related to refractive index) profile. In RFC, multiple calls to a forward solver are employed to predict clutter under certain ducting conditions, and these solutions are compared with new clutter observations to infer refractivity profiles. Such RFC methods frequently use the forward solver and so a full, 3D solution of Maxwell’s equations, can be computationally expensive; as a result, the Fourier split-step parabolic equation (SSPE) is commonly used as a fast and efficient forward model. However, even SSPE solutions may prove unwieldy within the context of RFC inversions for refractive index. As a result, efforts have focused on improving efficiency in optimization within the context of the RFC inversion: approaches in the literature include nonlinear least squares (Rogers et al., 2000), matched-field processing approaches (Gerstoft et al., 2000), Markov-chain Monte Carlo (Yardim et al., 2006), and Markov state-space models (Vasudevan et al., 2007). A review of RFC methods is available in Karimian et al. (2012).

Apart from RFC methods, approaches for constructing simplified forward models using observations obtained by sparsely sampling EM power within the MABL have emerged. Fountoulakis and Earls (2016) utilize blurring operators to approximate effects of the MABL, so that “just in time” estimates, for inferring duct parameters, may be obtained by manifold interpolation within a library of sparse proper orthogonal decomposition (POD) modes calculated offline from field observations. These field observations are sparsely sampled along a sinusoidal UAV flight path or a linear rocketsonde flight path. Gilles et al. (2019) bypasses the full forward model by decomposing the governing partial differential equation into few propagating trapped normal modes and solving an easier optimization problem posed on normal mode subspaces. In the context of this method, coverage is sparsely sampled, so as to be consistent with a bistatic case, in which a receiver is located downrange of a hypothetical transmitter.

In prior work, the current authors show that artificial neural networks (ANNs) can accurately and efficiently predict duct height from sparsely measured EM propagation factors (Sit and Earls, 2019). Similar to the above methods, the authors simulate coverage diagrams for duct heights of interest and utilize a series of sparse sampling schemes, that are consistent with practical deployment within bistatic contexts, to construct the dataset needed for training and testing. Parameters within the neural networks are then learned by minimizing the empirical risk on the training examples, and model generalizability is evaluated by assessing performance on test examples. While success was achieved in the foregoing work, in general, artificial neural networks are limited by small datasets in the duct characterization problem, and such models may be prone to overfit on the necessarily small training sets.

In the present paper, we propose using Gaussian process regression (GPR) to perform a similar task of predicting duct height from sparsely sampled propagation factors. GPR is a nonparametric, fully-Bayesian method that offers several advantages over other machine learning techniques, such as model interpretability and uncertainty quantification for predictions (Rasmussen and Williams, 2006). Using GPR, we tune the prior distribution over functions and subsequently calculate a predictive distribution to estimate duct height from propagation factors obtained via sparse bistatic sampling schemes.

This paper is outlined as follows. We begin by describing the forward model and EM sampling schemes that correspond to the different bistatic radar configurations. We then outline and describe the application of Gaussian process regression to our specific duct height prediction task. Finally, we discuss the results and offer a comparison of Gaussian process regression and artificial neural networks.

2 Forward Model

EM wave propagation between transmitter and receiver antennas can be modeled as an initial-value problem, using the Fourier split-step parabolic equation (SSPE) algorithm as an approximation to the time-independent Helmholtz wave equation (Ozgun et al., 2011):

$$\frac{\partial^2 \varphi}{\partial x^2} + \frac{\partial^2 \varphi}{\partial z^2} + k^2 n(z)^2 \varphi = 0 \quad (1)$$

where φ is the horizontal polarization of the electric field, k is the free-space wavenumber, and n is the refractive index. In the present work, our SSPE solution considers a 2D rectangular problem domain with maximum range (x) of 50km and altitude (z) of 113m, and grid spacings of 40m and 0.1m, respectively. The transmitter antenna is located at $x = 0km$, and parameters of its horizontally-polarized Gaussian antenna pattern, with radar signal frequency of 9.3

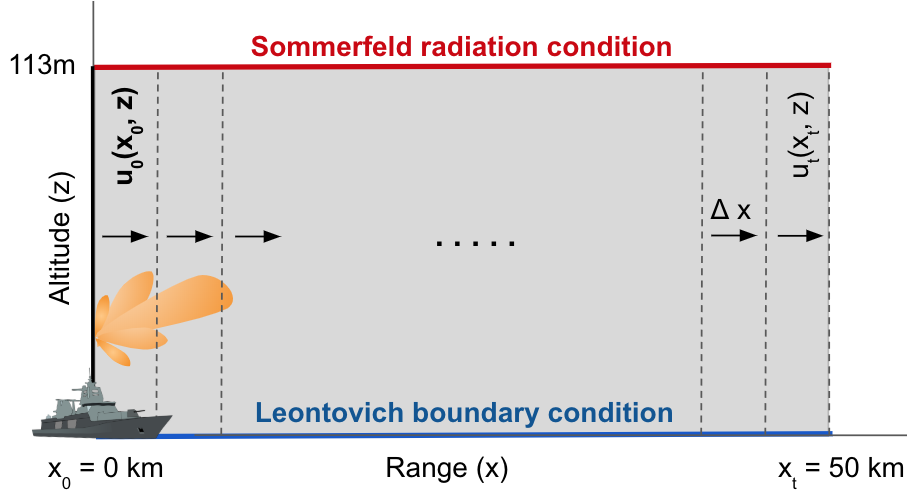


Figure 1: **Problem domain.** Domain of interest and associated boundary and initial conditions.

GHz, are used to specify the initial field at the left boundary. The field is propagated down range by a series of fast Fourier transformations, while satisfying the lower and upper boundary conditions. We use code from PETOOL (Ozgun et al., 2011) that has been adapted with the Leontovich surface impedance condition at the lower boundary (Gilles et al., 2019). The ocean free surface at $z = 0$ is assumed to be a flat, finite conductor with a homogeneous dielectric constant, where continuity of tangential components of the electric and magnetic fields is satisfied (Ryan, 1991). At infinity, the electric field is decayed to zero in the Sommerfeld radiation condition. Due to the electric field truncation at $z = 113m$, PETOOL approximates this condition at the upper boundary by extending the domain altitude and applying a Hanning window to remove non-physical reflections that result from this truncation.

The refractive index, n , in the Helmholtz equation (Eqn. 1) is height dependent, but is assumed to be constant in range. This index is the ratio of the velocity of EM propagation in free space to that in another medium, but often, we define another quantity called *refractivity*, $N = (n - 1)10^6$, to better study the small changes in the refractive index that characterize the MABL (Skolnik, 1980). Presence of atmospheric ducting results in a modified refractivity profile, which can be modeled as a log-linear curve for evaporation ducts:

$$M(z) = M_0 + c \left(z - z_d \ln \left(\frac{z + z_0}{z_0} \right) \right) \quad (2)$$

where M_0 is base refractivity, c is critical potential refractivity, z_0 is aerodynamic surface roughness of the ocean, and z_d is the duct height. With the following parameters as constants: $M_0 = 428.9M$ -units, $c = 0.13M$ -units/ m , and $z_0 = 0.00015m$, we solve the EM wave equation using SSPE for all considered duct heights, z_d , at every half meter between 2-40m in altitude, which encompasses practical evaporation duct height instances (Fountoulakis and Earls, 2016).

Finally, equipped with the EM wave solution, *propagation factors* (*i.e.* the features of interest in our problem) within the domain, collectively called the *coverage diagram*, can be calculated (Ozgun et al., 2011):

$$PF = 20 \log |u| + 10 \log x + 10 \log \lambda \quad (3)$$

where $u = \exp(-ikx)\varphi(x, z)$ is the reduced amplitude function for the parabolic equation and λ is the free-space wavelength.

2.1 EM sampling schemes

Propagation factors are sparsely sampled from within the coverage diagram to provide a practical context for collecting real-life bistatic radar measurements. We use three EM sampling schemes to construct three separate datasets, each consisting of an array of propagation factors (observation/input) for every considered duct height (label):

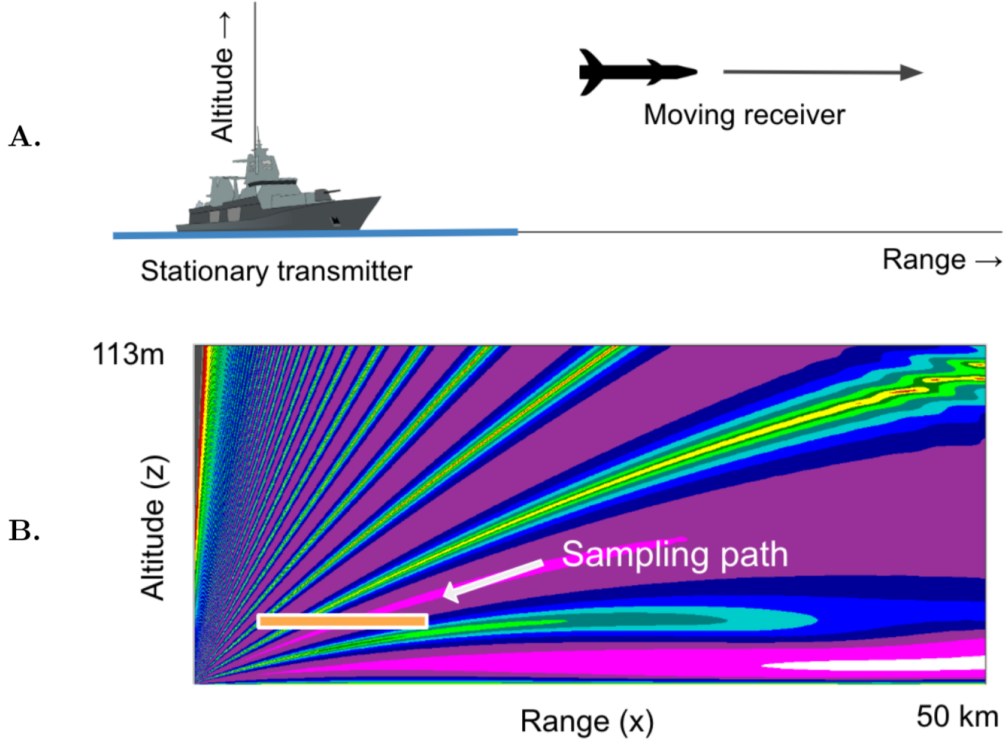


Figure 2: **EM Sampling Scheme 1.** Path is consistent with **A.** a stationary transmitter and moving receiver (RRSS), and is **B.** shown on representative coverage diagram.

(1) Stationary transmitter and moving receiver. We consider a stationary transmitter with antenna height of $h = 10m$ and angle of $\alpha = 0$, with respect to the horizontal, and a moving receiver attached to a *rocketsonde* (*i.e.* solid rocket propelled sensing system). This rocketsonde-receiver sampling system (RRSS) is flown at a constant altitude of $y = 21m$, and samples 250 evenly spaced propagation factors along a horizontal line between 5-15km in range. Please refer to Figure 2 for a depiction of this sampling path. This flight trajectory was arrived at as a result of an exhaustive sensitivity study aimed at uncovering short, flat sampling paths that lead to successful duct height inversions.

(2) Deterministically rocking transmitter and stationary receivers. We consider a rocking transmitter and stationary receivers mounted onto a vertical tower located at $x = 50km$ downrange. These receivers sample 30 equally spaced propagation factors between 0-30m in altitude. (Please refer to Figure 3 for a depiction of this sampling scheme.) The rocking is meant to be more closely aligned with the notion of a floating transmitter. To mimic deterministic rolling and heaving of the transmitter antenna, six observations are collected using discrete combinations of transmitter heights $h = 20m, 30m$ and antenna angles $\alpha = -0.5, 0, 0.5$, concatenated within an array of propagation factor measurements.

(3) Stochastically rocking transmitter and stationary receivers. Using the same sampling scheme as (2), to mimic stochastic rolling and heaving of the transmitter antenna, five observations are collected by sampling uniformly for transmitter antenna heights $h \sim U[20m, 30m]$ and antenna angles $\alpha \sim U[-0.5, 0.5]$, so as to form another array of measured propagation factors.

To create surrogate experimental results, we contaminate our propagation factor measurements with “severe” electronic sensor noise using additive Gaussian white noise: $\mathcal{N}(0, \sigma)$; $\sigma = 0.1\|x\|_\infty$, where standard deviation is 0.1 times the absolute value of the largest propagation factor from a given measurement array. However, it is noted that we train with more precise sensors than in testing (discussion in Section 3.4).

3 Gaussian Process Regression

Gaussian process regression (GPR) is a nonparametric fully-Bayesian method that performs inference in the space of assumed (prior) functions to ultimately arrive at the posterior predictive distributions at points where we would like

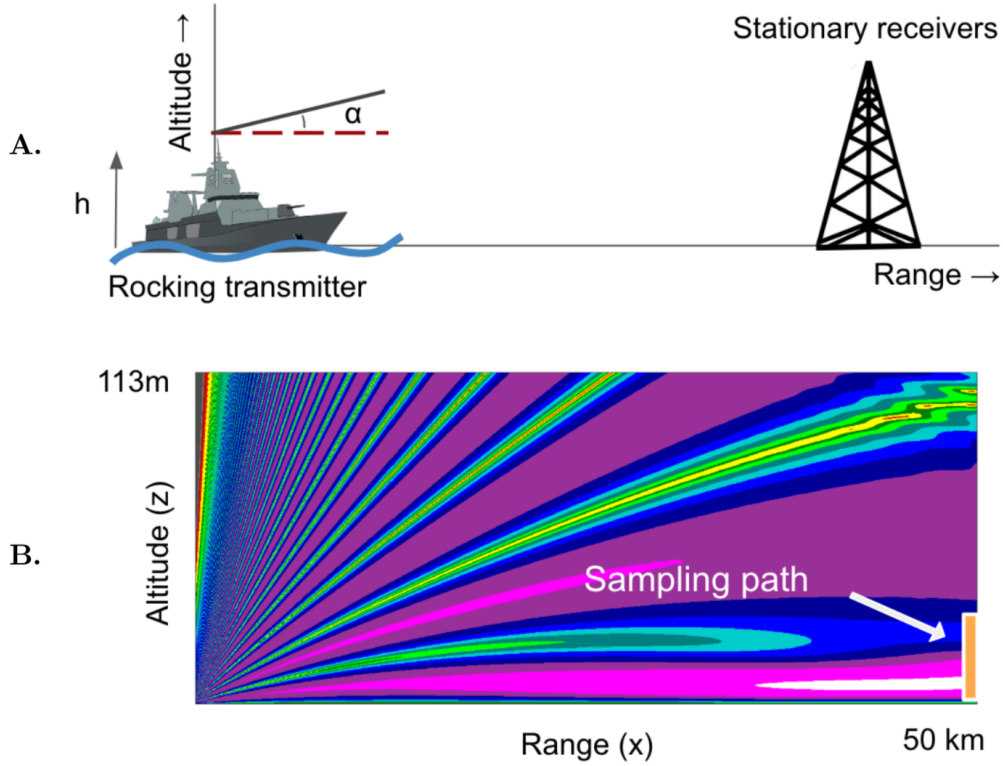


Figure 3: **EM Sampling Scheme 2**. Path is consistent with **A**, a rolling and heaving transmitter and stationary receivers mounted on a tower, and is **B**, shown on representative coverage diagram.

predictions. The joint prior distribution is specified as a Gaussian process, which is a collection of an uncountably infinite set of random variables such that any finite subset has a multivariate Gaussian distribution that can be specified using only mean, $m(x)$, and covariance, $k(x, x')$, functions (Rasmussen and Williams, 2006):

$$f(x) \sim \mathcal{GP}(m(x), k(x, x')) \quad (4)$$

If observation labels (on training points) are contaminated with independent and identically distributed (*i.i.d*) additive Gaussian white noise $\epsilon_y \sim \mathcal{N}(0, \sigma_n^2)$, its prior joint distribution can still be a Gaussian process, because the sum of two independent random variables from Gaussian distributions forms another Gaussian PDF that has mean and variance that are the sums of the two distributions. Thus, for noisy labels y , we can assume a Gaussian process with the following mean and covariance functions (Rasmussen and Williams, 2006):

$$y = f(x) + \epsilon_y \quad (5)$$

$$y \sim \mathcal{GP}(m(x), k(x, x') + \delta_{ij}\sigma_n^2) \quad (6)$$

where the noise variance, σ_n^2 , is set at 0.1, to correspond to the grid spacing in the altitude direction of our PETOOL model (as a way to encode ambiguity in the vertical resolution). The functions evaluated on training and test sets are thus, jointly Gaussian:

$$\begin{bmatrix} y \\ f_* \end{bmatrix} \sim \mathcal{N}\left(\begin{bmatrix} \mu \\ \mu_* \end{bmatrix}, \begin{bmatrix} K(X, X) + \sigma_n^2 I & K(X, X_*) \\ K(X_*, X) & K(X_*, X_*) \end{bmatrix}\right) \quad (7)$$

where y is the vector containing the noisy training labels, f_* is the vector of test predictions, μ is the vector of training label means, μ_* is the vector of test label means, X are the training observations, X_* are the test observations, and K is

the covariance kernel. Covariance functions are chosen by the analyst and their associated ‘‘hyperparameters’’ are tuned by maximizing the log marginal likelihood on the training observations. The posterior predictive distributions for new observations can then be calculated by conditioning the joint prior distribution on the data.

3.1 Covariance Kernel

The covariance kernel specifies the point-wise similarity within the GP and acts as a constraint on the distribution of functions in Gaussian process regression. A popular covariance kernel is the squared-exponential (SE) kernel (Rasmussen and Williams, 2006):

$$k_{SE}(x, x'; \theta) = \exp\left(-\frac{1}{2\ell^2}(x - x')^2\right) \quad (8)$$

SE is stationary and infinitely differentiable (Duvenaud, 2014). Within the family of kernels are tunable ‘‘hyperparameters’’ that further define the distribution of possible functions. The characteristic lengthscale, ℓ , in SE adjusts the smoothness of the functions (*i.e.* the longer the ℓ , the more smooth the functions, since a large ℓ indicates long range, point-wise similarity in the GP prior) (Rasmussen and Williams, 2006). Other common covariance kernels include constant, periodic, linear, and Matérn kernels. More expressive kernels can also be constructed by summing and multiplying these kernels. In the present work, we use the product of the constant kernel and the SE kernel, as our covariance kernel, so that the constant kernel scales the magnitude of the SE kernel, to encode the signal variance:

$$k(x, x'; \theta) = k_C(x, x'; \theta) * k_{SE}(x, x'; \theta) = \sigma_f^2 \exp\left(-\frac{1}{2\ell^2}(x - x')^2\right) \quad (9)$$

where x are the training observations, x' are the test observations, and σ_f^2 is the tunable signal variance. The initial value of the signal variance is specified as 1.0 with bounds of (1e-1, 1e3). The initial lengthscale of the SE kernel is specified as 10.0 with bounds of (1e-3, 1e3).

3.2 Model Selection

Model selection for GPR, typically referred to as model ‘‘training’’, is the process of selecting the family of covariance functions, and setting the free hyperparameters, θ (*e.g.* characteristic lengthscale ℓ in squared exponential functions). A common approach is to use an optimization algorithm to find hyperparameters that maximizes the log marginal likelihood. Marginal likelihood is the probability of the data, given model parameters (*i.e.* marginalize out the model parameters); thus, it inherently encodes a tradeoff between model complexity and fit (Rasmussen and Williams, 2006):

$$p(y|X) = \int P(y|X)p(f|X)df \quad (10)$$

$$\log p(y|X) = -\frac{1}{2}y^T(K + \sigma_n^2 I)^{-1}y - \frac{1}{2}\log|K + \sigma_n^2 I| - \frac{n}{2}\log 2\pi \quad (11)$$

where y are the labels, X are the observations, θ are the hyperparameters, and K is the covariance matrix emanating from the kernel function. When maximizing Eqn. 11, gradient-based optimization is preferred, because the inversion of the covariance matrix is performed only once and partial gradients of the log marginal likelihood with respect to the hyperparameters can easily be calculated (Rasmussen and Williams, 2006). Typically, inversion of this matrix within the calculation of the marginal likelihood is performed using Cholesky factorization for numerical stability. We use a computer memory efficient, quasi-Newton iterative method for bound-constrained optimization called L-BFGS-B within sci-kit learn (Pedregosa et al., 2011). The log likelihood is typically non-convex and as result, optimization is allowed to be restarted $n = 10$ times with different initializations, so as to identify reasonable parameters for the Gaussian process.

3.3 Prediction and Evaluation

The joint probability distribution on the training points and the test points is a multivariate Gaussian and thus, when conditioned on the observations, the resulting distribution, called the posterior predictive distribution, is also a multivariate Gaussian (Rasmussen and Williams, 2006):

$$f_*|X, y, X_* \sim \mathcal{N}(\bar{f}_*, \text{cov}(f_*)) \quad (12)$$

$$\bar{f}_* = \mu + K(X_*, X)[K(X, X) + \sigma_n^2 I]^{-1}(y - \mu_*) \quad (13)$$

$$\text{cov}(f_*) = K(X_*, X_*) - K(X_*, X)[K(X, X) + \sigma_n^2 I]^{-1}K(X, X_*) \quad (14)$$

As a result, GPR is able to provide a prediction, \bar{f}_* , which is the expected value from all possible functions, and its variance, which can be taken from the diagonal of the covariance matrix, $\text{cov}(f_*)$, for every desired test point. Calculation of the prediction and variance requires the inversion of the resulting covariance matrix, and again, for numerical stability, Cholesky factorization is often used.

Within the present work, GPR model predictions (*i.e.* duct heights) are evaluated using the mean squared error (MSE) metric, which measures the average squared difference between the predictions and labels.

$$MSE = \frac{1}{n} \sum_{i=1}^n (\bar{f}_{*i} - y_i)^2 \quad (15)$$

where n is the number of test points (where predictions are made), \bar{f}_{*i} are the model predictions (mean predicted duct heights), and y are the true labels (*i.e.* actual duct heights).

3.4 Observation Noise

Unlike noise on the training point labels, which can be easily incorporated into the Gaussian process, noise in the observations (*i.e.* inputs) is problematic. To obtain a prediction for a noise-contaminated input, we need to marginalize out the input distribution from the posterior predictive distribution, which results in a non-Gaussian distribution (Girard and Murray-Smith, 2005):

$$x = u + \epsilon_x \quad (16)$$

$$p(y|X, f, u, \Sigma_x) = \int p(y|X, f, x)p(x|u, \Sigma_x) \quad (17)$$

where u are the ground truth observations and Σ_x is a diagonal matrix containing the variance of the *i.i.d.* Gaussian white noise, ϵ_x , on the observation. Several approaches can be used to numerically or analytically approximate the integral (Eqn. 17). A numerical approximation can be obtained using Monte-Carlo sampling, which involves sampling the input distribution and mixing their Gaussian posterior predictive distributions to obtain a numerical estimation of the actual posterior predictive distribution (Girard and Murray-Smith, 2005):

$$p(y|X, f, u, \Sigma_x) \simeq \sum_{t=1}^T w_t p(y|X, f, x_t) = \sum_{t=1}^T w_t \mathcal{N}(\mu(x_t), \text{cov}(x_t)) \quad (18)$$

where T is the number of samples, w_t is the mixing proportion assigned the Gaussian (note: $\sum_{t=1}^T w_t = 1$), and x_t is a sampled input. For a given x_t , we compute the mean, $\mu(x_t)$, and covariance, $\text{cov}(x_t)$, of the Gaussian posterior predictive distribution. The resulting distribution from the mixture of Gaussians might not be Gaussian, but the mean and variance of the mixture distribution can still be calculated. The mean is the weighted mean of the means of the Gaussians, and the variance is the weighted variances of the Gaussians with additional terms that account for the weighted dispersion of the means of the Gaussians (Trailovic and Pao, 2002):

$$\mu_{mixture} = \sum_{t=1}^T w_t \mu(x_t) \quad (19)$$

$$\sigma_{mixture}^2 = \sum_{t=1}^T w_t (\sigma^2(x_t) + \mu(x_t)^2) - \mu_{mixture}^2 \quad (20)$$

The prediction can be approximated using the mean, and its 95% confidence interval can be generated using the variance (Eqn. 20). The desired true distribution can be approached with this approximate distribution by increasing the

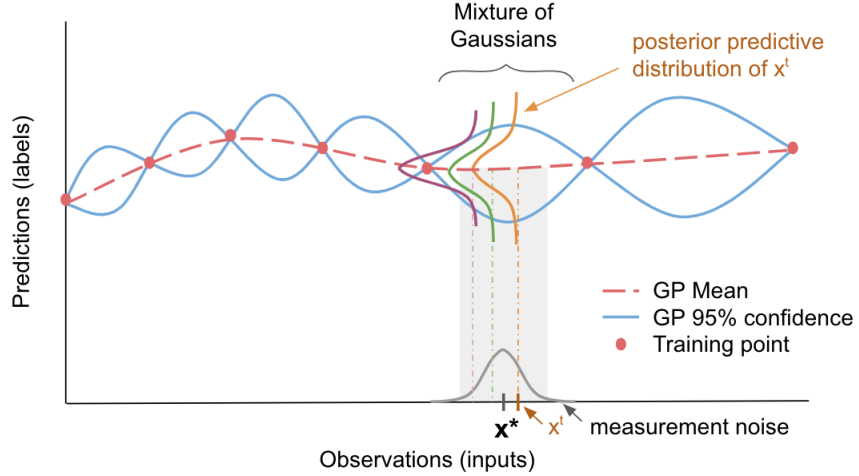


Figure 4: **Monte Carlo sampling of noisy observations.** A numerical estimation method that samples from the test point distribution and mixes the Gaussian posterior predictive distributions (on the labels) obtained for each sample, x^t , leading to an approximate posterior predictive distribution for x^* . (x^* is shown for a one-dimensional case for simplicity.)

number of samples; thus we choose large $T=1000$ with equal mixing proportions $w_t = \frac{1}{T}$ to estimate a “ground truth” distribution.

While other methods exist for arriving at the mixing proportions, we propose using an inverse-variance weighting scheme (Eqn. 21) for use when the number of observations of PF is small. In this way, the Gaussian with the smallest variance can be given the highest mixing proportion, w_t :

$$w_t = \frac{1/\sigma_t^2}{\sum_{t=1}^T 1/\sigma_t^2} \quad (21)$$

The above techniques do not account for noise on the training points, since considering a distribution over the training input is intractable in GPR (Mchutchon and Rasmussen, 2011). A method to circumvent this issue is to assume a deterministic input and recast the input noise as output noise to achieve the form of Eqn. 5. However, doing so causes the output variance to vary with the input, and the GP model now needs to account for the heteroscedasticity (*e.g.* the noisy input GP (NIGP) model in Mchutchon and Rasmussen (2011)). Thus, in the present paper, a more precise sensor is assumed for obtaining training observations, and the extreme electronic sensor noise is only applied on the testing observations.

4 Results

We use Gaussian process regression (GPR) to predict the duct height from both noise-free and noise-contaminated propagation factors. To observe the performance of GPR on small training sets, we vary the ratio of training points to testing points (Fig. 5). The end points of the dataset, 2m and 40m, are included in the training set, so that the model does not need to extrapolate at those points during inference.

For noise-contaminated propagation factors, we estimate the true posterior predictive distribution by calculating a numerical approximation using 1000 Monte-Carlo samples (approach shown in Fig. 4). From this approach, we obtain a “ground-truth” distribution, whose mean is the prediction from the noise-free measurement and variance is inflated to account for the input noise, for comparison with the naïve method, and the inverse-variance weighting method. In the naïve method, a single noise-contaminated measurement is assumed to be deterministic, and the posterior predictive distribution is calculated as if the measurement were a noise-free measurement. In the inverse-variance weighted method, detailed in Section 3.4, five mixing components are used with inverse-variance weighted mixing proportions (Eqn. 21). MSE on the duct height predictions, compared to the true label for all methods used, is shown in Table 1. Additionally, MSE on the predictions from the naïve approach and inverse-variance approach are compared to the

Table 1: MSE for Gaussian process regression predictions compared to true label

	Train/Test Ratio	Noise-Free	MC GT*	Naïve	IV**
CASE 1	80/20	4.84e-04	5.93e-03	1.37e-01	5.34e-02
	70/30	9.87e-03	9.07e-03	3.02e-01	5.30e-02
	60/40	1.09e-02	3.17e-02	2.81e-01	3.60e-02
	50/50	6.53e-03	5.17e-03	2.79e-01	6.14e-02
	40/60	4.93e-03	1.63e-02	3.45e-01	6.57e-02
	30/70	5.73e-03	5.83e-03	2.85e-01	7.93e-02
	Train/Test Ratio	Noise-Free	MC GT*	Naïve	IV**
CASE 2	80/20	2.08e-02	2.15e-02	5.90e-01	1.66e-01
	70/30	8.92e-02	8.98e-02	8.74e-01	2.18e-01
	60/40	1.39e-01	1.48e-01	8.29e-01	2.98e-01
	50/50	2.17e-01	2.93e-01	9.17e-01	4.57e-01
	40/60	3.13e-01	2.21e-01	6.31e-01	6.58e-01
	30/70	5.90e-01	5.86e-01	1.09	6.95e-01
	Train/Test Ratio	Noise-Free	MC GT*	Naïve	IV**
CASE 3	80/20	1.34e-02	1.80e-02	1.41	1.25e-01
	70/30	1.16e-02	1.28e-02	8.16e-01	2.39e-01
	60/40	2.00e-01	1.97e-01	1.43	4.44e-01
	50/50	1.37e-01	1.14e-01	1.45	2.75e-01
	40/60	3.28e-01	3.64e-01	1.37	4.74e-01
	30/70	3.30e-01	3.46e-01	1.47	6.85e-01

*MC GT - Monte Carlo Ground Truth

**IV - Inverse-variance weighting approach

“ground truth” duct height, shown in Table 2. For reference, root mean square error (RMSE) of 0.5m, which roughly corresponds to an MSE of $2.50e-1$ is judged to be good: given practical accuracy requirements in application.

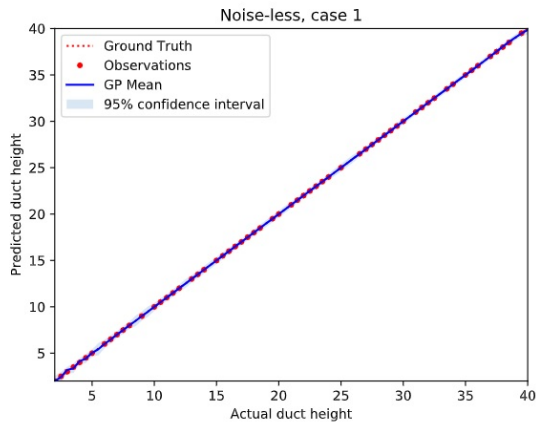
The variance of the predictions from the naïve case is similar to that from the ground truth (Figs. 6 and 7). This unexpected variance inflation can be attributed to the high dimensionality of the array of propagation factors (*i.e.* adding noise to every dimension can knock the test point further away from the training points in space). As can be seen in Table 3, the average Euclidean distance between the test inputs and their closest training input for the noise-contaminated test inputs is between 1.4 and 5.3 times further away.

While the improvement in variance is limited, the inverse-variance weighted method offers a large improvement to the predictions, decreasing the MSE (shown in the last two columns of Table 1 & 2) without the computational cost of MC sampling with 1000 samples (Table 3). Variability is expected due to random training/test splits and in the optimization of hyperparameters.

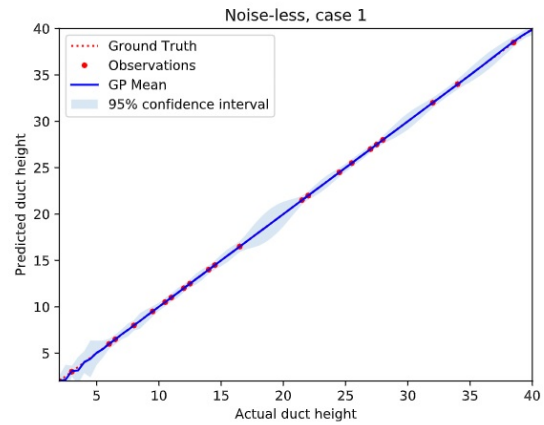
4.1 Timing

Both training and inference are performed using 4-cores of Intel i5 microprocessor having a clock speed of 2.7 GHz. Timing is calculated using the Python `time.clock()` method, which measures processor system time in seconds. Table 4 shows the time for training using `sci-kit learn`’s Gaussian process regression (Pedregosa et al., 2011) fit function and inference using the `predict` function. Inference time for obtaining the “ground-truth” distribution includes the inference time of the 1000 samples per test point, as well as extra computation for calculating the mean and variance of the posterior predictive distribution for each test point. Similarly, for the inverse-variance weighted approach, inference time includes the inference time of the five samples per test point as well as the extra computation. Training time (offline) in GPR is relatively modest, requiring fewer than two seconds of processor system time in all cases considered. Online inference takes fewer than two milliseconds for one random sample, and six milliseconds for five random samples using the inverse-variance weighting method. The additional time needed for the inverse-variance weighting method is modest, compared to the time required for ground truth estimation using MC sampling, which is on the order of hundreds of milliseconds. Since the MABL is assumed stationary over the timeframe of minutes (Rogers, 1996), our predictions certainly qualify as being “real-time”.

CASE 1

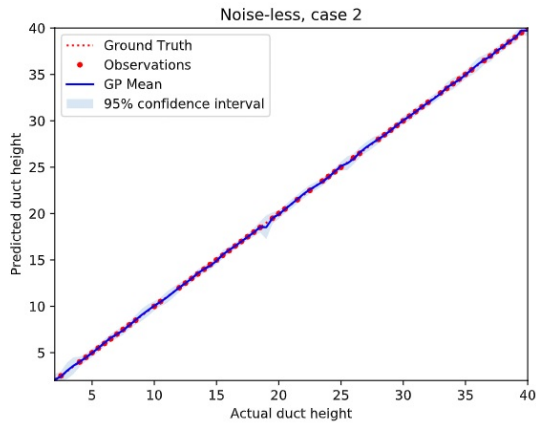


(a) 80/20 train-test split

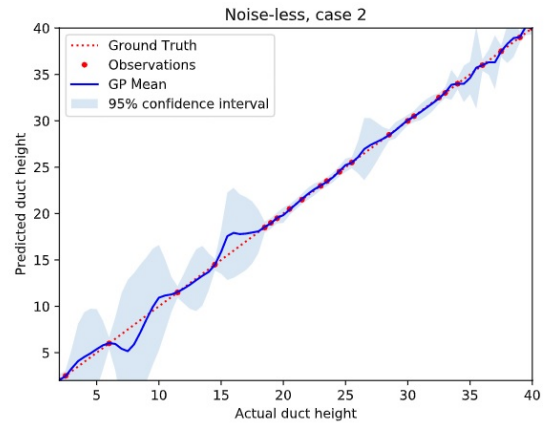


(b) 30/70 train-test split

CASE 2

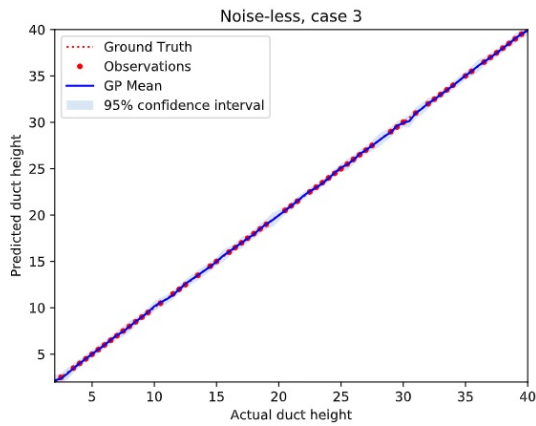


(c) 80/20 train-test split

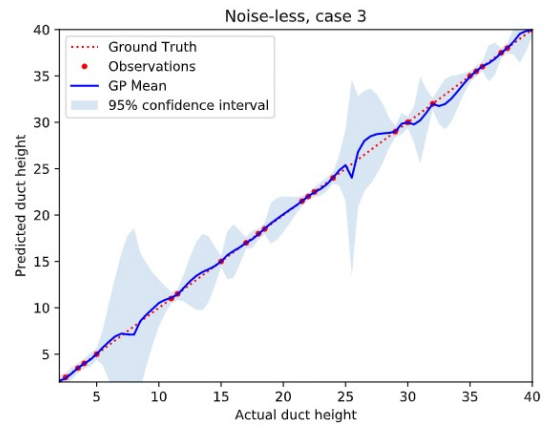


(d) 30/70 train-test split

CASE 3



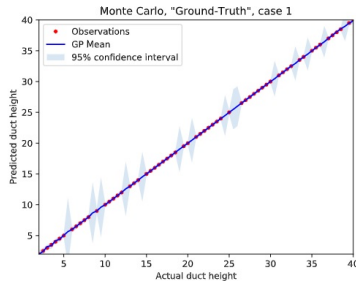
(e) 80/20 train-test split



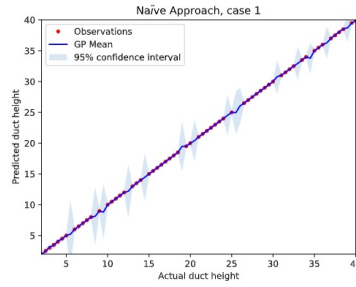
(f) 30/70 train-test split

Figure 5: GPR results from noise-free measurements using different train/test splits

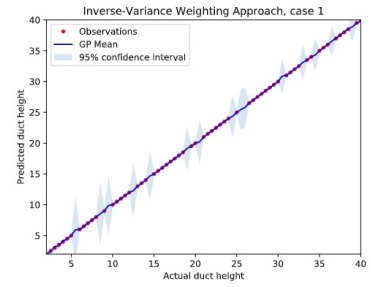
CASE 1



(a) Ground truth

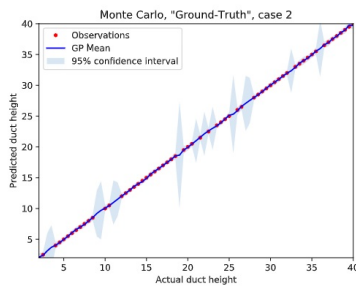


(b) Naive

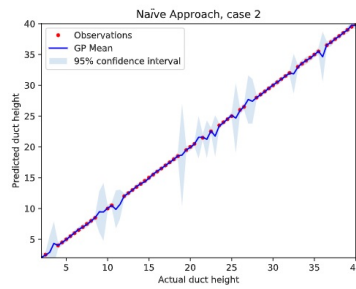


(c) Inverse-variance weighting

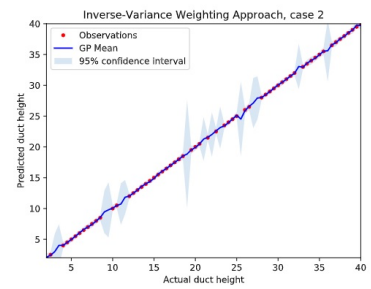
CASE 2



(d) Ground truth

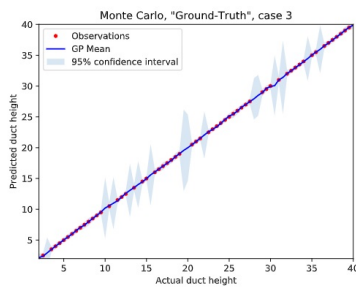


(e) Naive

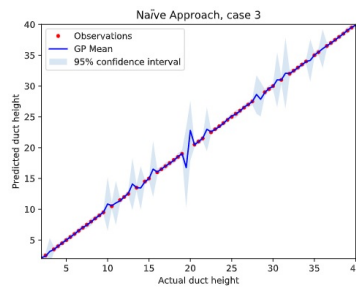


(f) Inverse-variance weighting

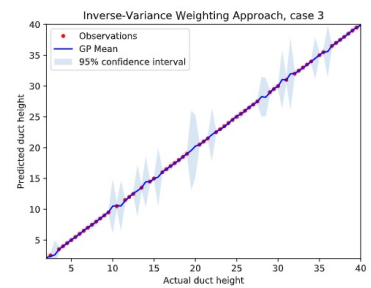
CASE 3



(g) Ground truth



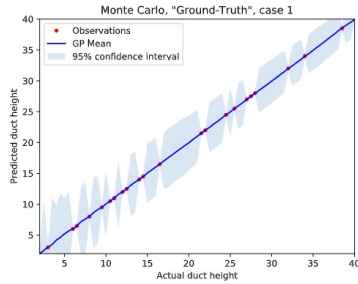
(h) Naive



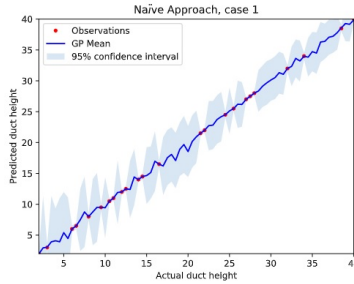
(i) Inverse-variance weighting

Figure 6: GPR results for noise-contaminated measurements using 80/20 split

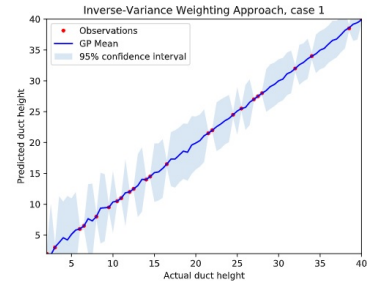
CASE 1



(a) Ground truth

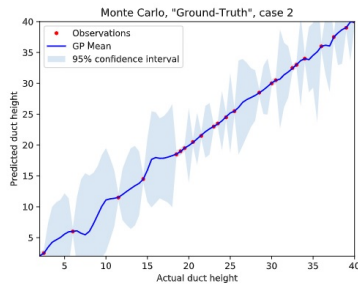


(b) Naive

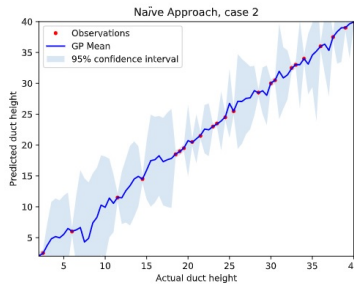


(c) Inverse-variance weighting

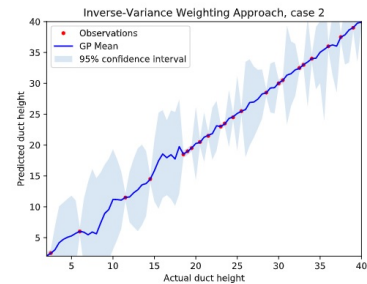
CASE 2



(d) Ground truth

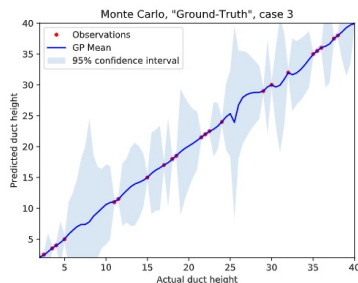


(e) Naive

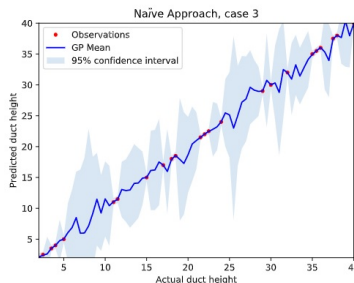


(f) Inverse-variance weighting

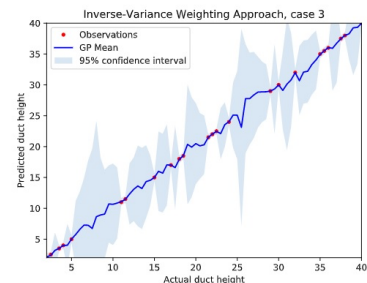
CASE 3



(g) Ground truth



(h) Naive



(i) Inverse-variance weighting

Figure 7: GPR results for noise-contaminated measurements using 30/70 split

Table 2: MSE for Gaussian process regression predictions (from naïve approach and inverse-variance weighting, IV, approach) compared to mean of “ground truth” distribution

	Train/Test Ratio	Naïve	IV
CASE 1	80/20	1.63e-01	4.66e-02
	70/30	2.62e-01	5.76e-02
	60/40	2.76e-01	6.33e-02
	50/50	2.83e-01	6.65e-02
	40/60	2.99e-01	4.52e-02
	30/70	2.80e-01	6.48e-02
	Train/Test Ratio	Naïve	IV
CASE 2	80/20	5.34e-01	1.25e-01
	70/30	6.29e-01	1.38e-01
	60/40	5.95e-01	1.33e-01
	50/50	7.34e-01	1.43e-01
	40/60	6.07e-01	1.98e-01
	30/70	4.07e-01	1.29e-01
	Train/Test Ratio	Naïve	IV
CASE 3	80/20	1.43	1.65e-01
	70/30	8.14e-01	2.08e-01
	60/40	1.00	1.98e-01
	50/50	1.20	1.76e-01
	40/60	1.01	1.24e-01
	30/70	1.05	1.98e-01

Table 3: Average Euclidean distance between test point and its closest training point.

	Train/Test Ratio	Noise-free	Noise-contaminated
CASE 1	80/20	6.85	36.6
	70/30	7.91	36.2
	60/40	9.87	40.0
	50/50	9.77	39.1
	40/60	11.8	39.1
	30/70	12.9	39.5
	Train/Test Ratio	Noise-free	Noise-contaminated
CASE 2	80/20	13.1	23.5
	70/30	15.9	28.3
	60/40	18.9	29.0
	50/50	18.1	28.8
	40/60	18.5	29.2
	30/70	23.8	33.3
	Train/Test Ratio	Noise-free	Noise-contaminated
CASE 3	80/20	11.6	23.4
	70/30	12.5	23.4
	60/40	14.1	25.9
	50/50	15.1	26.3
	40/60	21.0	30.3
	30/70	24.3	33.7

Table 4: Fitting and Inference Times (seconds)

	Train/Test Ratio	No.*	Training	NF** & naïve	MC	IV
CASE 1	80/20	62	1.12	7.60e-04	2.78e-01	3.70e-03
	70/30	54	6.44e-01	6.67e-04	3.65e-01	2.98e-03
	60/40	47	6.51e-01	1.71e-03	4.35e-01	4.93e-03
	50/50	39	8.39e-01	7.63e-04	4.50e-01	5.29e-03
	40/60	31	5.67e-01	9.37e-04	4.50e-01	2.96e-03
	30/70	24	3.46e-01	8.18e-04	4.02e-01	3.36e-03
	Train/Test Ratio	No.*	Training	NF** & naïve	MC	IV
CASE 2	80/20	62	5.43e-01	1.31e-03	2.21e-01	3.30e-03
	70/30	54	5.84e-01	1.36e-03	2.87e-01	4.00e-03
	60/40	47	5.71e-01	1.50e-03	3.42e-01	3.46e-03
	50/50	39	5.68e-01	1.56e-03	3.54e-01	2.91e-03
	40/60	31	6.64e-01	8.49e-04	3.47e-01	3.01e-03
	30/70	24	4.58e-01	1.58e-03	3.13e-01	3.80e-03
	Train/Test Ratio	No.*	Training	NF** & naïve	MC	IV
CASE 3	80/20	62	7.66e-01	4.76e-04	1.78e-01	2.73e-03
	70/30	54	7.01e-01	7.77e-04	2.43e-01	3.23e-03
	60/40	47	5.45e-01	1.10e-03	2.90e-01	3.96e-03
	50/50	39	6.06e-01	1.33e-03	3.06e-01	3.88e-03
	40/60	31	5.97e-01	5.56e-04	2.71e-01	2.46e-03
	30/70	24	3.30e-01	5.24e-04	2.69e-01	1.83e-03

*No. of training points

**NF - Noise-free

4.2 Comparison to Neural Networks

Previously, we trained artificial neural networks to approximate a mapping between arrays of sparsely sampled propagation factors and duct heights (Sit and Earls, 2019). The small dataset, inherent in the duct height prediction, poses a challenge in training these networks. As such, we used a stochastic optimization scheme with small, shallow networks to mitigate overfitting on the training dataset. When the inputs are contaminated with Gaussian noise, we additionally augment each point in the training set 200 times. The search for optimal parameters in neural networks is confined by the non-convexity of the loss surface. Presence of local minima is not an issue for larger networks, because they are typically of high quality, but for small networks, getting trapped at low quality local minima is a concern (Choromanska et al., 2015).

Unlike artificial neural networks, Gaussian process regression is able to approximate this mapping using few training examples, given that the training set represents the entire range of the dataset. Thus, Gaussian process regression is beneficial in cases where data collection is sparse, which is inherent in our duct characterization problem. “Training” time is considerably faster than that of artificial neural networks, which requires multiple forward and backward passes through the network to update parameters. However, inference time can be slower depending on the number of training points, m , because in Gaussian process regression, calculating the mean of the posterior predictive distribution requires inversion of the $K(X, X) + \sigma_n^2 I$ matrix, which dominates the calculation with $\mathcal{O}(m^3)$ computational complexity. Artificial neural networks, on the other hand, require $\mathcal{O}(n)$ complexity during inference, where n is the number of test points. Thus, one should take into consideration the trade-offs between artificial neural networks and Gaussian process regression when selecting a method for the duct characterization problem where inference time is very important.

5 Conclusion

Gaussian process regression can be a powerful tool for problems limited by small datasets, such as the duct characterization problem. We show that GPR is able to accurately predict duct height from an array of propagation factors that is sparsely sampled within a context that is consistent with bistatic radar systems. We varied the number of training points: 62 (80/20 train test split) to 24 (30/70 train test split), to observe the performance of GPR on small datasets. For noise-contaminated propagation factors, we show that the inverse-variance weighing approach performs better in the duct height estimation than the naïve approach, but that the naïve approach can be sufficient if data are limited, due to inflated model uncertainty. From these results and recorded inference times, Gaussian process regression provides suitable, “real-time” inference of duct height.

6 Acknowledgments

Datasets and code for GPR are available at <https://github.com/nonlinearfun/gpr-em-ducting>. The authors gratefully acknowledge ONR Division 331 & Dr. Steve Russell for the financial support of this work through grant N00014-19-1-2095.

References

- Bean, B. R. and Dutton, E. J. *Radio Meteorology*. Dover books on electronics and related areas. Dover, Washington D.C., 1968.
- Choromanska, A.; Henaff, M.; Mathieu, M.; Ben Arous, G., and Lecun, Y. The loss surface of multilayer networks. *Artificial Intelligence and Statistics*, 2015.
- Duvenaud, D. *Automatic Model Construction with Gaussian Processes*. Phd thesis, University of Cambridge, 2014.
- Fountoulakis, V. and Earls, C. Inverting for maritime environments using proper orthogonal bases from sparsely sampled electromagnetic propagation data. *IEEE Transactions on Geoscience and Remote Sensing*, 54(12):7166–7176, 2016. ISSN 0196-2892. doi: 10.1109/TGRS.2016.2597138.
- Gerstoft, P.; Gingras, D. F.; Rogers, L. T., and Hodgkiss, W. S. Estimation of radio refractivity structure using matched-field array processing. *IEEE Transactions on Antennas and Propagation*, 48(3):345–356, 2000. ISSN 0018-926X. doi: 10.1109/8.841895.
- Gilles, M. A.; Earls, C. J., and Bindel, D. A subspace pursuit method to infer refractivity in the marine atmospheric boundary layer. *IEEE Transactions on Geoscience and Remote Sensing*, pages 1–12, 2019. ISSN 0196-2892. doi: 10.1109/TGRS.2019.2900582.
- Girard, A. and Murray-Smith, R. Gaussian processes: Prediction at a noisy input and application to iterative multiple-step ahead forecasting of time-series. In *Switching and learning in feedback systems*, pages 158–184. Springer, 2005.
- Karimian, A.; Yardim, C.; Hodgkiss, W.; Gerstoft, P., and Barrios, A. Estimation of radio refractivity using a multiple angle clutter model. *Radio Science*, 47, 2012. doi: 10.1029/2011RS004701.
- Lowry, A. R.; Rocken, C.; Sokolovskiy, S. V., and Anderson, K. D. Vertical profiling of atmospheric refractivity from ground-based gps. *Radio Science*, 37(3):13–1–13–19, 2002. doi: 10.1029/2000RS002565.
- Mchutchon, A. and Rasmussen, C. E. Gaussian process training with input noise. In Shawe-Taylor, J.; Zemel, R. S.; Bartlett, P. L.; Pereira, F., and Weinberger, K. Q., editors, *Advances in Neural Information Processing Systems*, pages 1341–1349. Curran Associates, Inc., 2011.
- Ozgun, O.; Apaydin, G.; Kuzuoglu, M., and Sevgi, L. Petool: Matlab-based one-way and two-way split-step parabolic equation tool for radiowave propagation over variable terrain. *Computer Physics Communications*, 182:2638–2654, 2011. doi: 10.1016/j.cpc.2011.07.017.
- Pedregosa, F.; Varoquaux, G.; Gramfort, A.; Michel, V.; Thirion, B.; Grisel, O.; Blondel, M.; Prettenhofer, P.; Weiss, R.; Dubourg, V., and others, . Scikit-learn: Machine learning in python. *Journal of machine learning research*, 12: 2825–2830, 2011.
- Rasmussen, C. E. and Williams, C. K. I. *Gaussian Processes for Machine Learning*. The MIT Press, Massachusetts Institute of Technology, 2006.
- Rogers, L. T. Effects of the variability of atmospheric refractivity on propagation estimates. *IEEE Transactions on Antennas and Propagation*, 44:460–465, 1996.
- Rogers, L. T.; Hattan, C. P., and Stapleton, J. K. Estimating evaporation duct heights from radar sea echo. *Radio Science*, 35(4):955–966, 2000. ISSN 1944-799X. doi: 10.1029/1999RS002275.
- Ryan, F. J. *User’s guide for the VTRPE (Variable Terrain Radio Parabolic Equation) computer model, Technical Report 1456*. Naval Ocean Systems Center, San Diego, California, 1991.
- Sikora, D. T. and Ufermann, S. Marine atmospheric boundary layer cellular convection and longitudinal roll vortices. In Jackson, C. and Apel, J., editors, *Synthetic aperture radar marine user’s manual*, pages 321–330. NOAA, Washington D.C., 2004.
- Sit, H. and Earls, C. J. Characterizing evaporation ducts within the marine atmospheric boundary layer using artificial neural networks. *Radio Science*, 2019. IN REVIEW.
- Skolnik, M. I. *Introduction to Radar Systems*. Electrical Engineering Series. McGraw-Hill, 1980. ISBN 9780070579095.

- Trailovic, L. and Pao, L. Y. Variance estimation and ranking of gaussian mixture distributions in target tracking applications. In *Proceedings of the 41st IEEE Conference on Decision and Control*, volume 2, pages 2195–2201 vol.2, 2002. doi: 10.1109/CDC.2002.1184857.
- Vasudevan, S.; Anderson, R. H.; Kraut, S.; Gerstoft, P.; Rogers, L. T., and Krolik, J. L. Recursive bayesian electromagnetic refractivity estimation from radar sea clutter. *Radio Science*, 42(2), 2007. doi: 10.1029/2005RS003423.
- Willitsford, A. and Philbrick, C. Lidar description of the evaporative duct in ocean environments. *Proceedings of SPIE - The International Society for Optical Engineering*, 2005. doi: 10.1117/12.620948.
- Yardim, C.; Gerstoft, P., and S. Hodgkiss, W. Estimation of radio refractivity from radar clutter using bayesian monte carlo analysis. *IEEE Transactions on Antennas and Propagation*, 54:1318 – 1327, 2006. doi: 10.1109/TAP.2006.872673.